A Novel Detection Algorithm for Impulse Spike Interferences in Cross-Track Infrared Sounder Short-Wave Spectral Radiance

Xin Jin, Banghua Yan, Ninghai Sun, Flavio Iturbide-Sanchez, *Senior Member, IEEE*, and Yong Chen

***Abstract*—Due to deficiencies in the operational spike detection, many moderate and strong impulse spike interferences constantly remain nondetected in the cross-track infrared sounder (CrIS) sensor data record (SDR) data at the short-wave infrared (SWIR) band over the South Atlantic Anomaly (SAA) region. This study characterizes imaginary radiance spectrum features in the presence of four intensities of spikes at three different hitting locations through radiative transfer model simulations. It is found that periodic ringing patterns appear in the imaginary spectral radiance. Following it, we establish a novel spike detection algorithm based on the spiky feature of power spectral density (PSD) in detrended and normalized imaginary SWIR CrIS spectral radiances. The performance of the algorithm is assessed by applying it to the multiple years of the SNPP and NOAA-20 CrIS full spectral resolution (FSR) radiance data. Approximate 300 and 500 spike events per day are detected for SNPP and NOAA-20 CrIS individually. The spikes can obviously increase the uncertainty in brightness temperature measurements at SWIR window channels that is determined by hitting location of the interferogram arms and the impulse intensities. Strong impulse spikes can trigger spectral radiance uncertainty by several times in SWIR window channels. Even the weakest impulse event can increase spectral radiance uncertainty by 4% in SWIR window channels. In addition, our simulations and one case study of CrIS data show that the spikes can degrade the quality of the CrIS data at the SWIR band with the largest impact at absorbing channels and the smallest at the window channels. The resultant brightness temperature change are 3 K for absorbing channels and up to 1 K for window channels in the SWIR band, demonstrating the significance flagging the CrIS data that are contaminated by the moderate and strong spikes that are missed in the operational data processing.**

***Index Terms*—Digital signal processing, Fourier transform infrared, hyperspectral sensors, low earth orbit satellites.**

Manuscript received July 19, 2021; accepted August 31, 2021. Date of publication September 8, 2021; date of current version September 22, 2021. This work was supported by the JPSS contract ST1330-7-Q-050. *(Corresponding author: Xin Jin.)*

Xin Jin is with the Science Systems and Applications, Inc., Lanham, MD 20706 USA (e-mail: xin.jin@noaa.gov).

Banghua Yan, Flavio Iturbide-Sanchez, and Yong Chen are with the Center for Satellite Applications and Research, National Environmental Satellite, Data, and Information Service, National Oceanic and Atmospheric Administration, College Park, MD 20740 USA (e-mail: banghua.yan@noaa.gov; flavio.iturbide@noaa.gov; yong.chen@noaa.gov).

Ninghai Sun is with the Global Science and Technology, Inc., Greenbelt, MD 20770 USA (e-mail: ninghai.sun@noaa.gov).

Digital Object Identifier 10.1109/JSTARS.2021.3110257

I. Introduction

THE cross-track infrared sounder (CrIS) is one of the instruments that onboard the Suomi National Polar-orbiting Partnership (SNPP) and the National Oceanic and Atmospheric Administration (NOAA)-20 satellites. It provides hyperspectral radiances of either 1305, i.e., normal spectral resolution (NSR), or 2211, i.e., full spectral resolution (FSR) frequencies emitted from the earth's surface and its atmosphere, covering three infrared bands: long-wave infrared (LWIR), mid-wave infrared (MWIR), and short-wave infrared (SWIR). This instrument finishes a scan in 8 s, which consists of 34 field-of-regards (FORs) of measurements, where 30 FORs are reserved for scanning the earth scene (ES), two FORs looking at the internal calibration target (ICT), and two FORs looking at the deep space (DS) scene. Each FOR contains a three-by-three field-of-view (FOV) array [1]. Table I lists the spectral, sampling, and decimation factor specifications of the CrIS instrument. The spectral radiance sensor data record (SDR) data of the CrIS instruments onboarding SNPP and NOAA-20 satellites are processed by the interface data processing segment (IDPS) and are distributed to the user community through the office of satellite and product operations (OSPO), product distribution and access (PDA), and NOAA's comprehensive large array-data stewardship system (CLASS).

The accuracy of the CrIS spectral radiance data is important for many applications, including the numerical weather prediction, inter-sensor calibration, atmospheric component retrieval, and climate process studies [2]–[6]. Currently, the CrIS SDR data quality is widely recognized in the user community due to a mature calibration algorithm [7] and a set of comprehensive data quality control system [1]. However, a problem still remains in the CrIS SDR data at the SWIR band due to the occurrence of impulse spikes over the South Atlantic anomaly (SAA), which is associated to the effect of cosmic particle interaction with the sensitive instrument detectors and associated electronics [8]. Currently, extremely strong spikes can be detected by using the bit-trim mask table in the onboard data processing, but such strong spike events are rare [9]. Another impulse spike detection method is developed in the ground data calibration system by comparing two sides of the interferogram around the zero path difference (ZPD) since the spike destroys its symmetry feature [10]. This method was applied only between October 3, 2018 and December 15, 2018, since it caused many false alarms in MWIR,

TABLE I
SPECTRAL SPECIFICATION OF SNPP CRIS INSTRUMENT[1] [1]

Frequency Band	Spectral Range (cm^{-1})	Unapodized Inband channel	Interferogram sampling bins[2]	Spectral resolution (cm^{-1})	Effective Maximum Path Difference (cm)
LWIR	650 to 1095	717(717)	874(874)	0.625(0.625)	0.8(0.8)
MWIR	1210 to 1750	437(869)	530(1052)	1.25(0.625)	0.4(0.8)
SWIR	2155 to 2550	163(637)	202(808)	2.5(0.625)	0.2(0.8)

[1]The NOAA-20 CrIS has the same specification as SNPP CrIS, and the data in parentheses correspond to the FSR SDR
[2]These numbers have been updated several times since SNPP mission.

DS, and ICT moving window size (e.g.,[1]). As a result, many undetected spikes remain in the current operational CrIS SDR product degrading the data quality (see the following analysis in this study). This calls for the development of a new method to detect moderate and strong spikes contaminating the quality of the CrIS data.

In this study, we present a method for detecting the spike-contaminated data, using SWIR CrIS imaginary spectral radiance because the spike-triggered current is of the similar magnitude of the SWIR detector current [10]. This includes the analysis about features of simulated CrIS FSR ES spectral radiance at the SWIR band in the presence of spikes with variable intensities and locations in the interferogram domain by using a line-by-line radiative transfer model (LBLRTM) [11]. With this analysis, we establish a novel algorithm to detect the impulse spike interferences through the power spectral density (PSD) pattern of the SWIR imaginary spectral radiance. Furthermore, the new algorithm is applied to the SNPP and NOAA-20 CrIS FSR SDR radiance data between 2016 and 2021 to assess the performance of the algorithm and its impact on the quality of the CrIS SDR data products.

Section II simulates features of the ES imaginary spectral radiance at the SWIR band in the presence of spikes with variable intensities and locations in the interferogram domain. Section 3 presents the spike detection algorithm. In Section IV, the new spike algorithm is applied to the SNPP and NOAA-20 CrIS SDR radiance data to assess the performance and impact of the algorithm on the quality of the CrIS SDR data products. Summary and conclusions are given in Section V.

II. CHARACTERISTICS OF SPIKE-CONTAMINATED ES IMAGINARY RADIANCE

The impulse spike in the interferogram domain can be described as the following form:

$$I_{impulse}(x) = A \cdot \delta(\mathrm{x} - \mathrm{x}_0). \tag{1}$$

Here, δ is the discretised Dirac delta function, A is the intensity, and x-x_0 represents the distance between the impulse spike and ZPD, which is frequently used to describe the hitting location in the interferogram domain.

[1][Online]. Available: https://www.star.nesdis.noaa.gov/smcd/icvs_metrics/status/J01/CrIS_FSR//2019/07/20190708_ICT_WindowSize_alltime_AVG_MW.png

The Fourier transform of interferogram with an impulse spike with a limited interval α is [12]

$$\mathrm{F}(\mathrm{x}) = \frac{1}{2a} + \frac{1}{a}\sum_{n=1}^{n_{max}} \left(\cos\left(n\frac{[\pi]}{a}x_0\right)\cos\left(n\frac{[\pi]}{a}x\right) + \sin\left(n\frac{[\pi]}{a}x_0\right)\sin\left(n\frac{[\pi]}{a}x\right)\right). \tag{2}$$

Equation (2) shows that the impact of an impulse spike on the interferogram domain can spread over every frequency in the spectral domain. It is necessary to investigate features of spikes with different intensities and locations on spectral radiance at CrIS wavelengths. However, it is difficult to conduct this analysis using the measured CrIS data. The LBLRTM, covering the wavenumber scale from 0 to 3500 cm^{-1} in 0.0005 cm^{-1} step, is used to simulate the CrIS top-of-atmospheric spectral radiance in the presence of various types of spikes. The input atmospheric model is the U.S. 1976 standard atmosphere. The simulated spikes consist of three hitting locations: the edge, the harmonic, and the near center region of interferogram. Each of them has impulse spikes at four levels of intensities, i.e., 1.3, 2, 4, and 6 times of the original radiometric value without the spike's contamination (also named as the reference value), representing weak, moderate, strong, and very strong impulse events, respectively. The simulated radiance is further converted to the interferogram domain and truncated to the CrIS spectral resolution for the analysis about features and impacts of spikes (see Fig. 1).

Fig. 2(a)–(c) displays the simulated interferogram in the presence of the spikes at three locations correspondingly. Only part of each interferogram is plotted to highlight the spike events. The maximal absolute values triggered by the impulse spikes are located at 20th sampling bin for the edge events, 124th for the harmonic events, and 380th for the near center events. At each location, the four intensities of spikes, as defined above, are included. The nonimpacted original value (1x) is also plotted for reference. Figs. 2–4 display the imaginary part of the simulated spectral radiance corresponding to the spikes in Fig. 2(a)–(c), respectively. They also include the impacts of spike on the radiance, which is defined as the brightness temperature (BT) deviations against the simulated ES radiance without spike contamination. As shown in the figures, certain ringing patterns appear in the imaginary spectral radiance as impulse noise changes the phase of spectral radiance. The frequency and intensity of the ringing patterns vary with the intensity

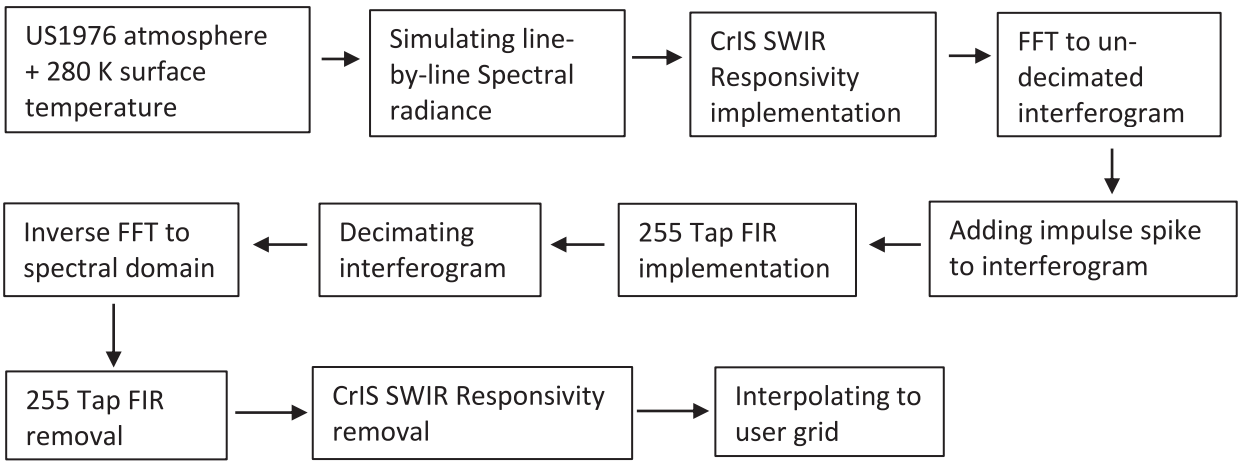

Fig. 1. CrIS SWIR impulse spike simulation flowchart.

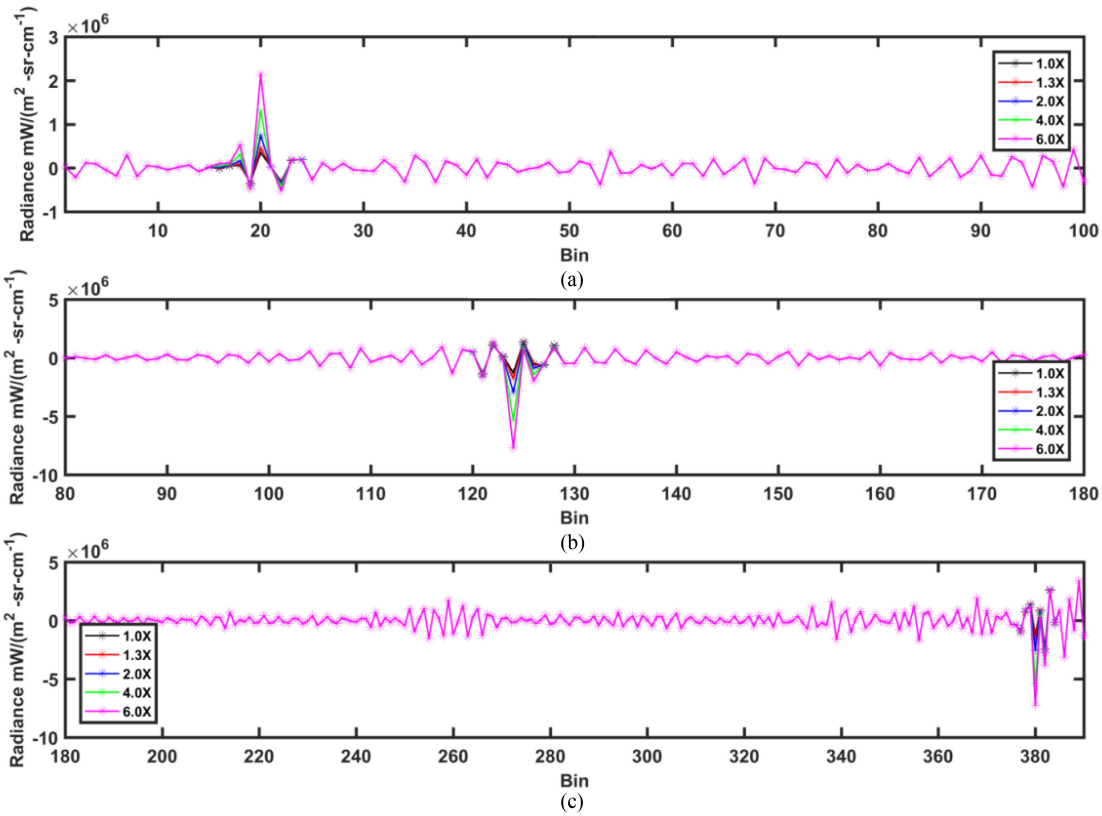

Fig. 2. Simulated impulse noise events at three locations on the interferogram. (a) Edge. (b) Harmonic. (c) Near center. The original value (1x) is also plotted for comparison.

and location of spikes in the interferogram, as summarized below.

First, imaginary radiance spectrum at the SWIR band presents a lower frequency ringing pattern as the spike moves to the center of interferogram (left panels in Fig. 3). Those spike intrusions result in certain BT biases against the BTs without the spike contamination, depending on wavelength (right panels in Fig. 3). The CO_2 absorption continuum between 2230 and 2380 cm^{-1} at the CrIS SWIR band are much more sensitive than window channels. If the impulse is a weak one, i.e., only 30% higher than the reference value, the biggest change of BT is about 0.6 K at around 2380 cm^{-1} that is the border between the absorption continuum and window zone. For most window channels, the uncertainty caused by impulse noise is less than 0.06 K, lower

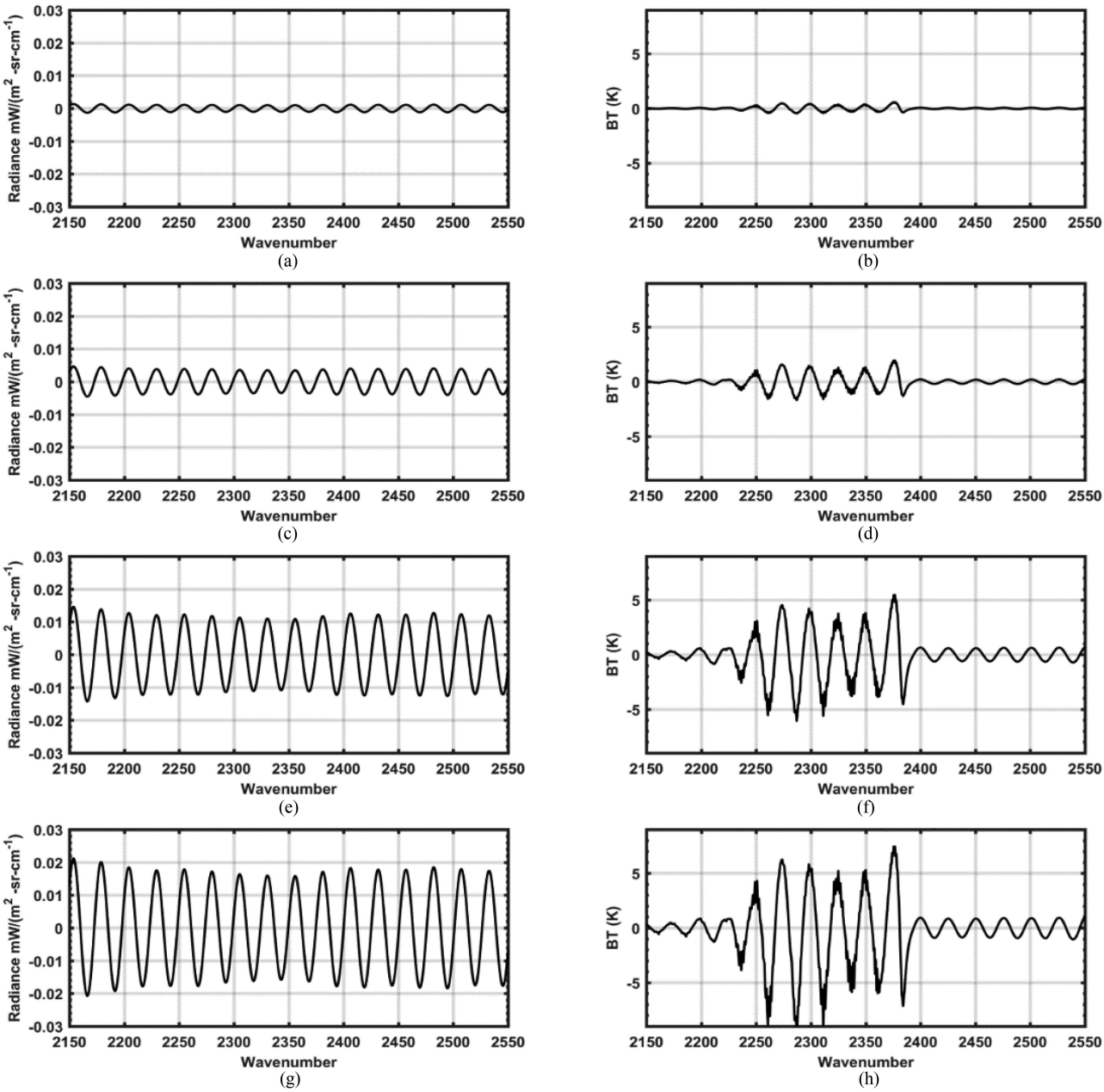

Fig. 3. Imaginary part of simulated ES radiances (Left column) and the BT difference (right column) compared to reference in case of impulse noise events occurring near the interferogram center with difference intensities. (a)–(b) Weak. (c)–(d) Moderate. (e)–(f) Strong. (g)–(h) Very strong.

than the 3-sigma radiance uncertainty, which is 0.1 K declared in [13]. However, if the impulse amplitude is doubled, the maximal BT difference is about 2 K at the absorbing channels and 0.2 K at window channels. If the impulse amplitude is much larger, such as 4 and 6 times higher than the original, the maximal BT difference could go up to 5 and 9 K at absorbing channels, respectively, 0.6 and 1 K at window channels, respectively.

Second, the spike introduces much higher frequency ringing pattern in the imaginary spectral radiance (Fig. 4 left panels) as it hits the edge part of the interferogram. Regarding to the BT bias, both window and absorption zones became more ringing but the amplitude was shrunk. The biggest difference still happens at around 2380 cm^{-1}, and its amplitude varies with the intensity of spikes, 0.2, 0.5, 2, and 3 K for weak, moderate, strong, and very strong cases, respectively. For most of the window zone, the amplitude of difference is nearly ten times smaller: 0.02, 0.08, 0.2, and 0.3 K, respectively. Comparing to the near center spike events, the impact of edge events is generally lower, where only strong and very strong impulse events could cause significant biases.

Thirdly, the impulse impact is complicated when the impulse spike hits the ES interferogram harmonic zones that are caused by the selective absorbing feature of the atmospheric components, as given in Fig. 5. Comparing with Figs. 3 and 4, the ringing is more evenly distribute in each wavenumber. If the impulse amplitude is weak, the ringing amplitude is around

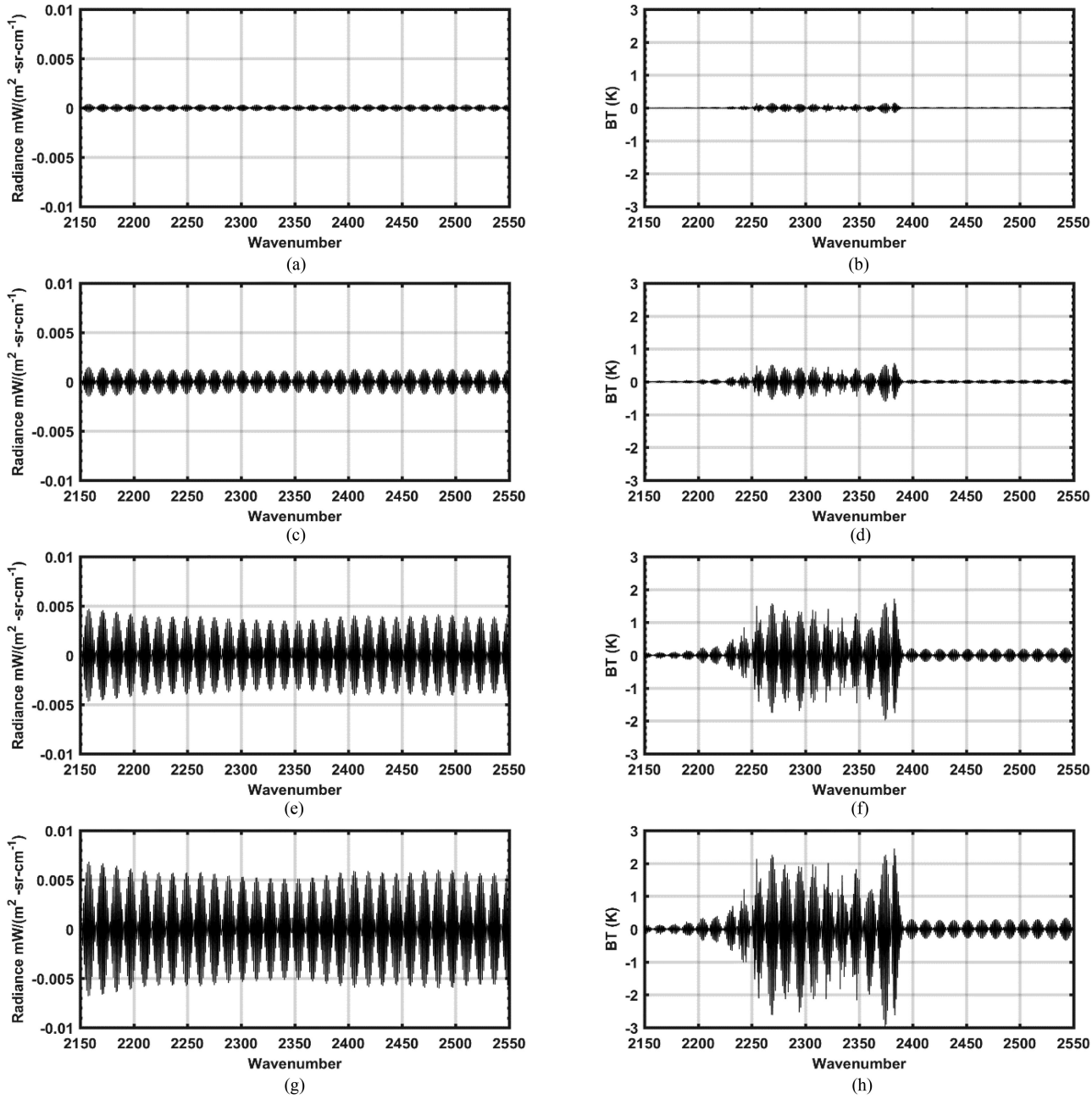

Fig. 4. Same as Fig. 3 but the impulse noise is near the edge of interferogram.

0.1 K for window zone, and the maximal difference is about 1 K at around 2380 cm^{-1}. The impact is significantly greater than that happened in either the edge or near the center. If the impulse amplitude is 2/4/6 times of the original, the maximal BT bias could reach 4/12/40 K in the absorbing channels and 0.3/0.6/1 K in window channels.

Table II summarizes the BT differences in the presence of spikes with diverse magnitudes at three locations in the interferogram based upon the results in Figs. 2–4. The BT differences are determined by the location of spikes. If the spike is weak, i.e., only 30% greater than the original value, the maximal caused BT bias is on the order of 1 K. If the spike amplitude is doubled, its impact is less than 0.3 K if it happens in the edge part. However, this impact becomes larger if it happens in either the harmonic or near the center. If the spike amplitude is more than double of the original value then they will produce significant differences against radiative transfer model simulations. It is also found, according to the simulation, the most sensitive channels are those near the 2380 cm^{-1}, i.e., the boundary between CO_2 absorbing continuum and window channels.

Therefore, the above simulation analyzes have shown that spike interferences can cause a series of periodic ringing patterns with different occurrence frequency and intensity in the contaminated imaginary spectral radiance. The BT differences due to most of the simulated spike interferences are nonnegligible with the largest impact at absorbing channels near the 2380 cm^{-1}.

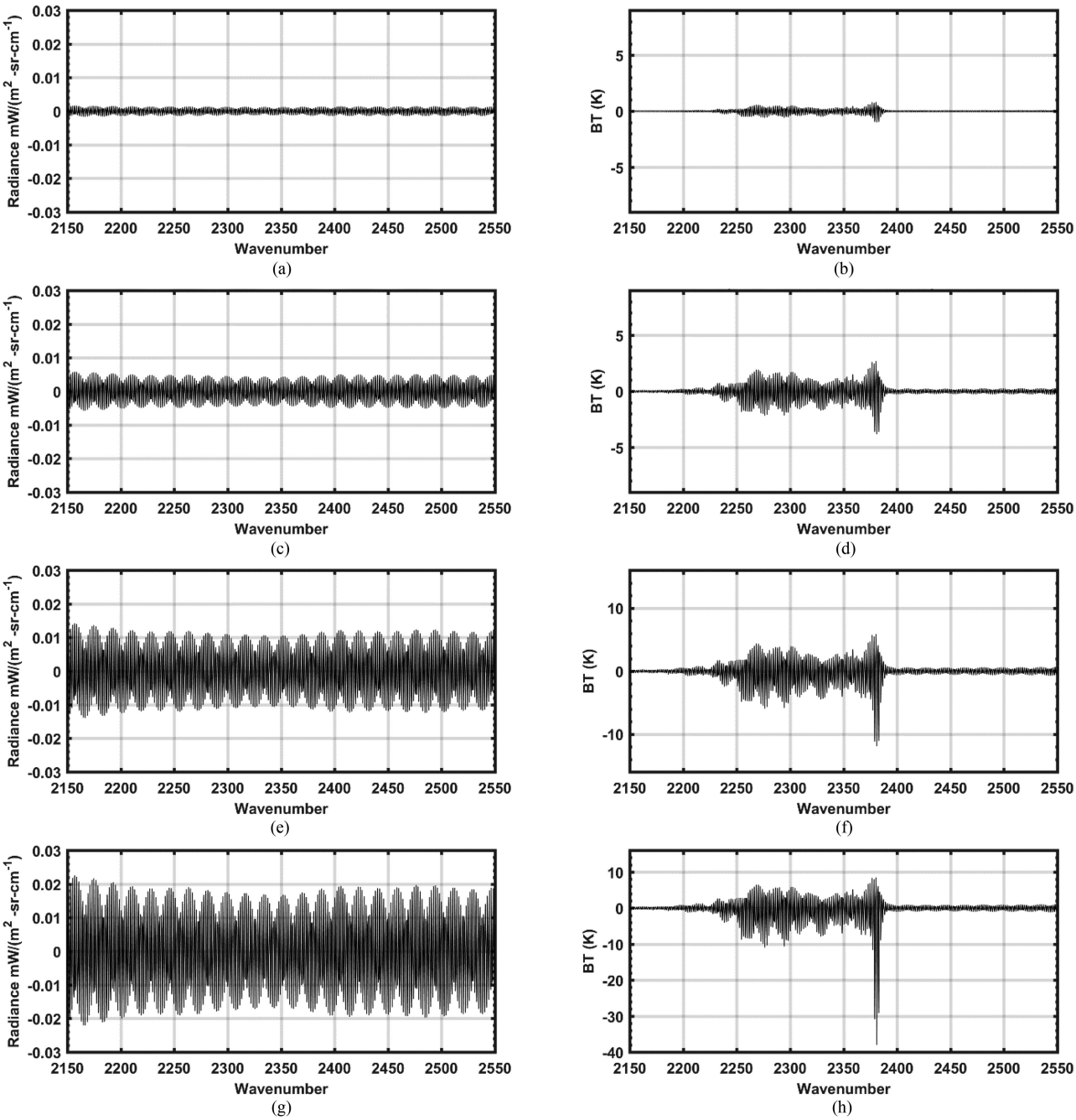

Fig. 5. Same as Fig. 3 but the impulse noise is within the harmonic zone of interferogram.

TABLE II
BT UNCERTAINTY (K) TRIGGERED BY SIMULATED IMPULSE NOISE

Amplitude	Edge		Harmonic		Near Center	
	Absorbing	Window	Absorbing	Window	Absorbing	Window
Weak (1.3x)	0.2	0.02	1	0.1	0.6	0.06
Moderate (2x)	0.5	0.08	4	0.3	2	0.2
Strong (4x)	2	0.2	12	0.6	5	0.6
Very Strong (6x)	3	0.3	40	1	9	1

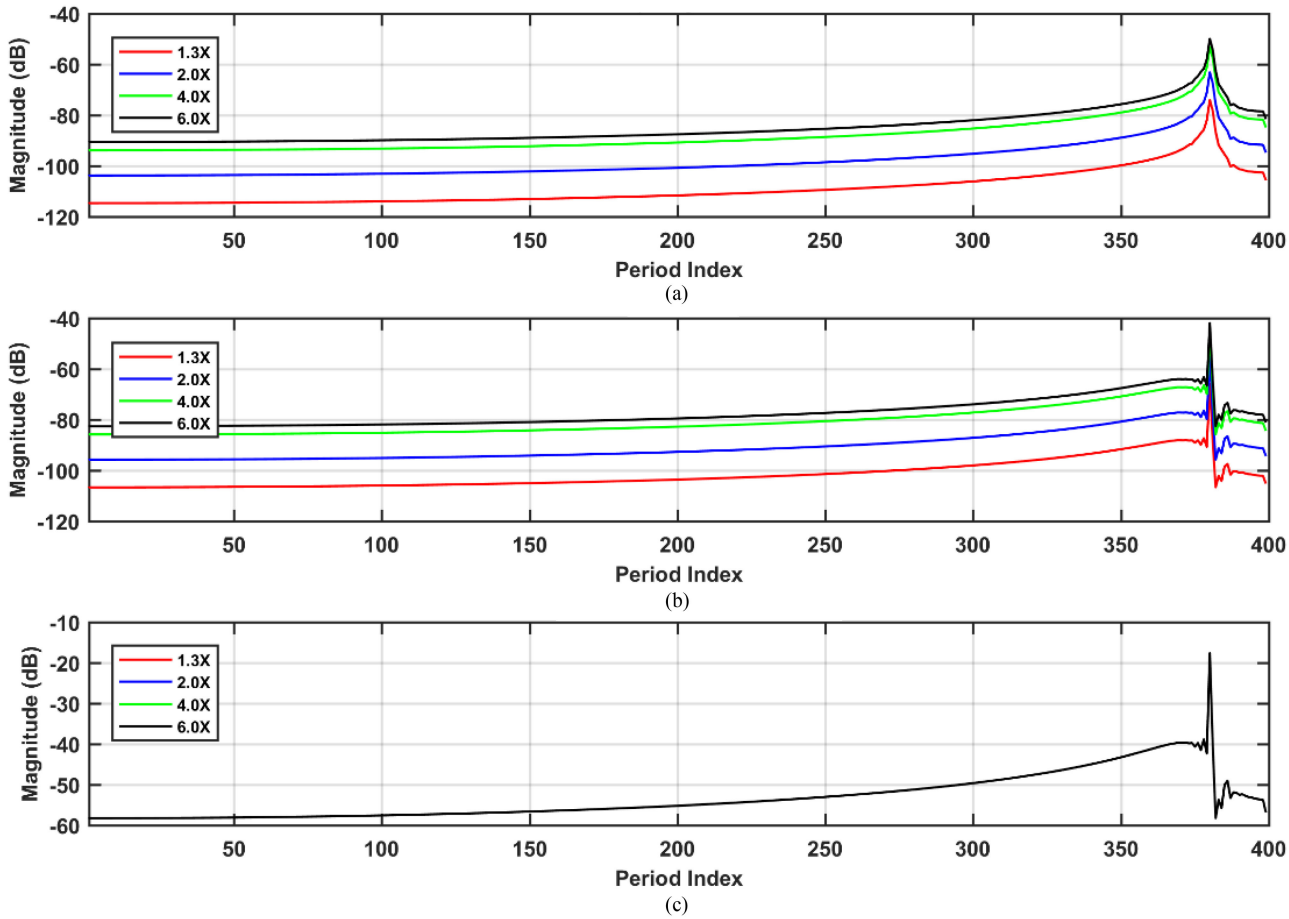

Fig. 6. PSD of simulated imaginary radiance with impulse noise at the interferogram edge area. (a) Directly calculated from simulated imaginary radiance. (b) Lag-1 difference applied. (c) Both lag-1 difference and normalization applied. Note that there is no difference among all four lines after normalization in Fig. 6(c).

This indicates the significance to flag observed CrIS data at the SWIR band that are contaminated by spikes for the user community. A spike detection algorithm is presented in next section.

III. Development of Spike Detection Algorithm

As analyzed above, the spikes-contaminated radiance shows a periodic ringing pattern in the imaginary part of the radiance spectrum. This period ringing pattern is more clearly revealed in corresponding PSD distribution. The detection algorithm in this study is thus developed based on manipulation of imaginary radiance PSD, as described below.

The PSD distribution of imaginary radiance is sensitive to periodic features introduced by impulse noise on the interferogram domain. Fig. 6(a) illustrates the PSD distribution of imaginary radiance spectrum corresponding to the edge cases in Fig. 4. The peak of the PSD varies with the intensity of the spike, and the spiky pattern is quickly flattened and is less clearly visible. To enhance the spiky feature, two additional reprocessing are applied to the original PSD data, i.e., the Lag-1 difference and normalization. The processing of Lag-1 difference added a little distortion to the original spiky shape but the spike-caused peak is well preserved, and the normalization processing makes sure the spike magnitude derived from different impulse events is comparable to each other. From Fig. 6(b)–(c) displays so-processed PSD distributions of the simulated imaginary radiance in Fig. 6(a). Even for the case with the weakest spikes, the normalized PSD [see Fig. 6(c)] still shows a strong spiky pattern, indicating that the renormalized PSD is more sensitive to periodic features introduced by the impulse noise on the interferogram domain. The processing procedure for generating the normalized PSD distribution is described in Appendix A.

In practice, the real interferogram always has some shift of ZPD location so its imaginary spectrum cannot be zero even, although, there are no spike events, which is different from the simulated data. Other than ZPD shift, the real interferogram also contains spectral noise. Fig. 7 is PSD of the NOAA-20 CrIS FSR SDR granule whose beginning time is 02:57:43 on February 1, 2019, where the Lag-1 difference and normalization are applied to the imaginary radiance spectral before applying the PSD. This granule contains 1080 SWIR spectral radiance samples and some of them are hit by impulse noise events. As a result, the measured imaginary spectral data are much noisier than the simulations.

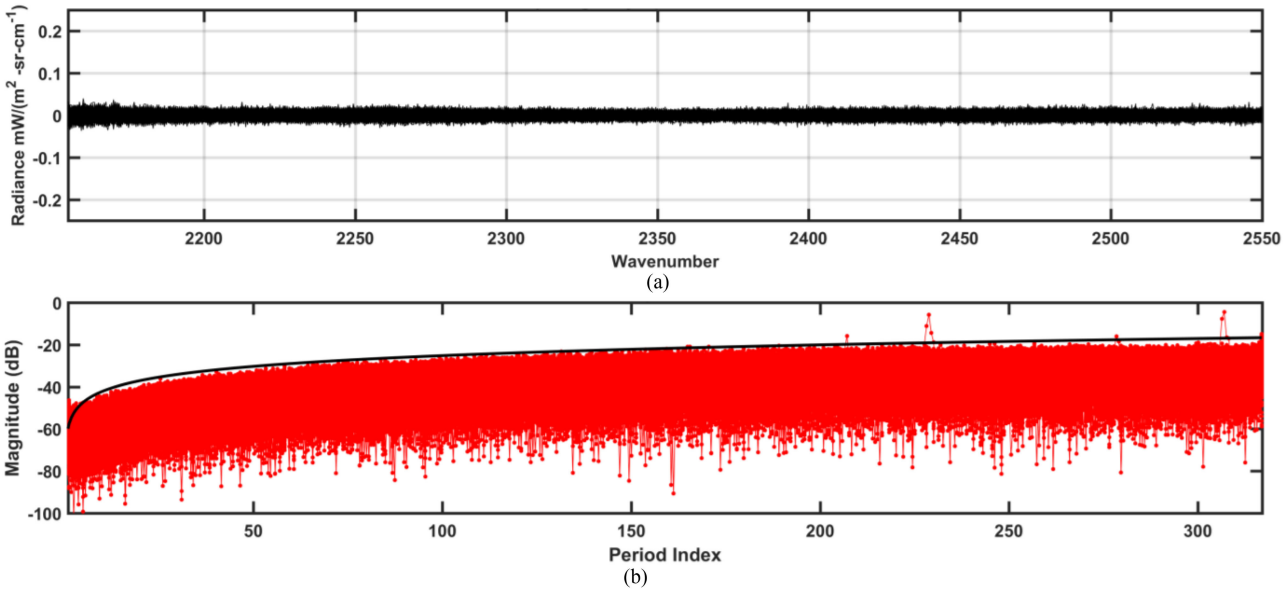

Fig. 7. (a) SWIR imaginary spectral radiance and (b) their logarithmic PSD with data from a NOAA-20 CrIS FSR SDR granule started at 02:57:43, February 1, 2019, which consists of 1080 spectrum with two impulse events.

In this study, a fitting curve is added to this PSD plot in Fig. 7(b) to define the threshold between nominal cases and outliers caused by impulse noise in the following spike intrusion detection algorithm. By analyzing PSD of CrIS data in the presence of possible spikes, the PSD show similar features as found in Fig. 7.

The NPP and NOAA-20 CrIS radiance measurement of February 1, 2019 is used as an initial training dateset to find out the coefficients in the fitting equation. Here is the definition of this fitting curve

$$Y = 7.384 * log(X) - 61.19. \tag{3}$$

Here, X is the incremental period values, ranged from 0 to 317 with a resolution 0.62. Any PSD series with values above this line at each period bin could indicate an impulse noise event. The features of the PSD should change with the data. The following three quality control (QC) criteria are demonstrated to efficiently eliminate false alarms caused by hot scenes by applying (3) to the CrIS data in February 2019 and evaluating the geographic pattern of the spike for each case as follows:

1) ignore the results for the first ten period values;
2) ignore the result for the last period value;
3) detect at least two continuous outliers above the threshold line, with the maximal distance between outliers and the threshold line larger than five units.

Fig. 8 shows the flow chart of the spike detection processing in combination with the fitting equation and the three criteria.

IV. Application of the Algorithm to the CrIS Data

The above simulations have shown that the spikes can significantly affect the quality of CrIS data at the SWIR band particularly in the absorption channels. Thus, it is of interest to assess if the new algorithm can detect CrIS data that are contaminated by the spikes with moderate or strong intensities. It is very difficult to quantify the impact of the spikes on the quality of measured CrIS SDT data since various error sources are mixed with the actual ES radiance or brightness temperatures. Even so, some attempts are conducted to quantify the impact of the spikes on the data quality below.

A. Detection of Spike-Contaminated CrIS Data

First, we apply the algorithm to a few single granules of the CrIS SDR data in the presence of two specific events, i.e., false spike (e.g., sun glint) and double spike occurrence. Fig. 9 displays imaginary radiance spectra of one granule that was partially within sun glints and corresponding PSD by following the processing of the algorithm in Fig. 8. The imaginary spectral radiance contains stronger signal pattern compared with those unaffected, but no impulse noise events are detected by the detection method [see Fig. 9(b)]. This indicates that the algorithm is less affected by the imaginary spectral radiance distortion due to reasons other than impulse spikes.

Occasionally, more than one impulse hit the sensor when it samples an interferogram, as shown in Fig. 10. In this case, one hits the second harmonic zone and the other hits the zone near the ZPD. The corresponding imaginary spectral radiance shows some periodic feature rather than the random noise and both impulse spikes are caught by our spike detection algorithm.

In addition to the above two specific cases, this algorithm is further applied to a long history of CrIS FSR data to assess daily occurrence frequency of spike intrusions in the data. Fig. 11 indicates the time series of the number of detected spike events for the SNPP and NOAA-20 CrIS FSR SDR data during the period between January 1, 2016 and February 28, 2021. The daily occurrence of impulse noise events is between 300 and 500 for most days, i.e., 0.01–0.02% out of the total number of

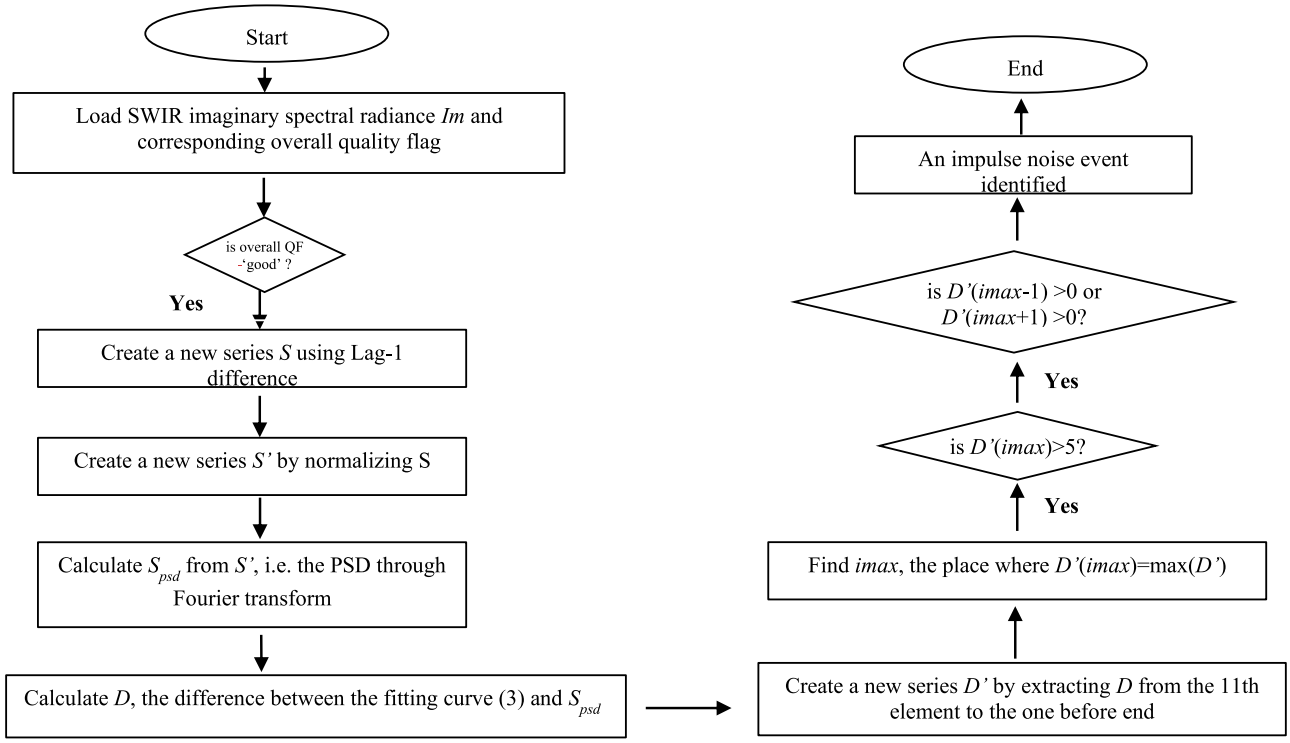

Fig. 8. Impulse noise detection flowchart.

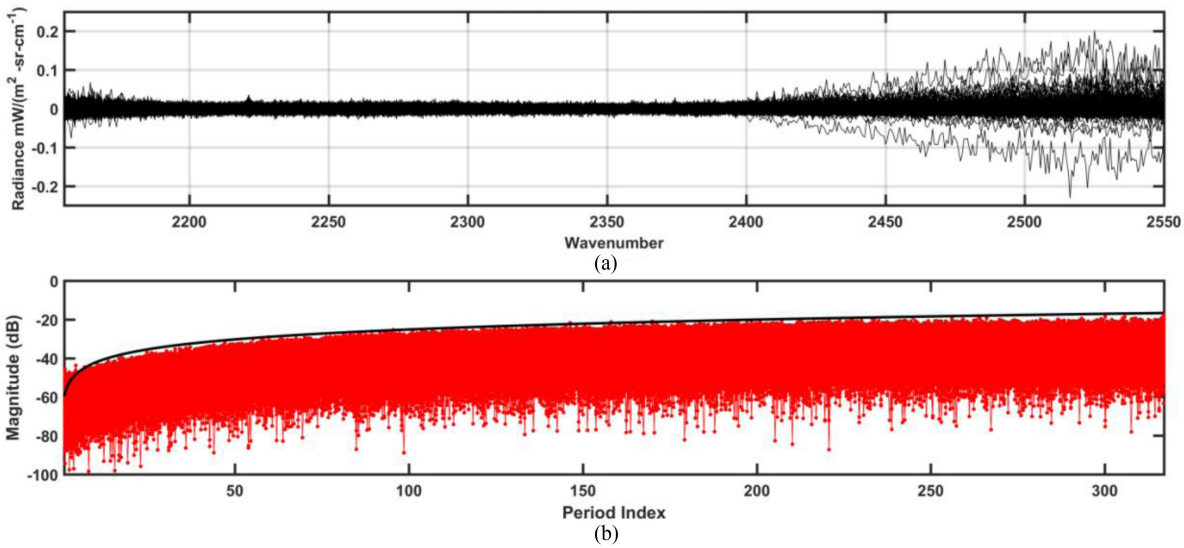

Fig. 9. Same as Fig. 7 but with data from a NOAA-20 CrIS FSR SDR granule started at 05:13:11, February 20, 2019.

SWIR ES pixels collected for each day could be contaminated by the impulse noise.

Some unusual events are found on Fig. 11. A sharp spike is identified on the SNPP time series around September 10, 2017. It is caused by a strong solar flare, which significantly increases the number of spike events [14]. The impulse spike events increases suddenly on September 10, 2017 and reaches the highest value on the next day, confirming that the solar flare is the major contributor of charged particles hitting the spacecraft.

Another sudden increase of spike events during the last quarter of 2018 for both instruments was caused by the implementation of the first version of impulse spike correction algorithm. Due to the unoptimized setting of threshold value to detect impulse spikes on the interferogram domain, this algorithm triggered many false alarms on the near kernel part and/or the harmonic part of the ES interferogram, producing many false ringing radiance cases [15]. An improved version is developed and ready to implement [16].

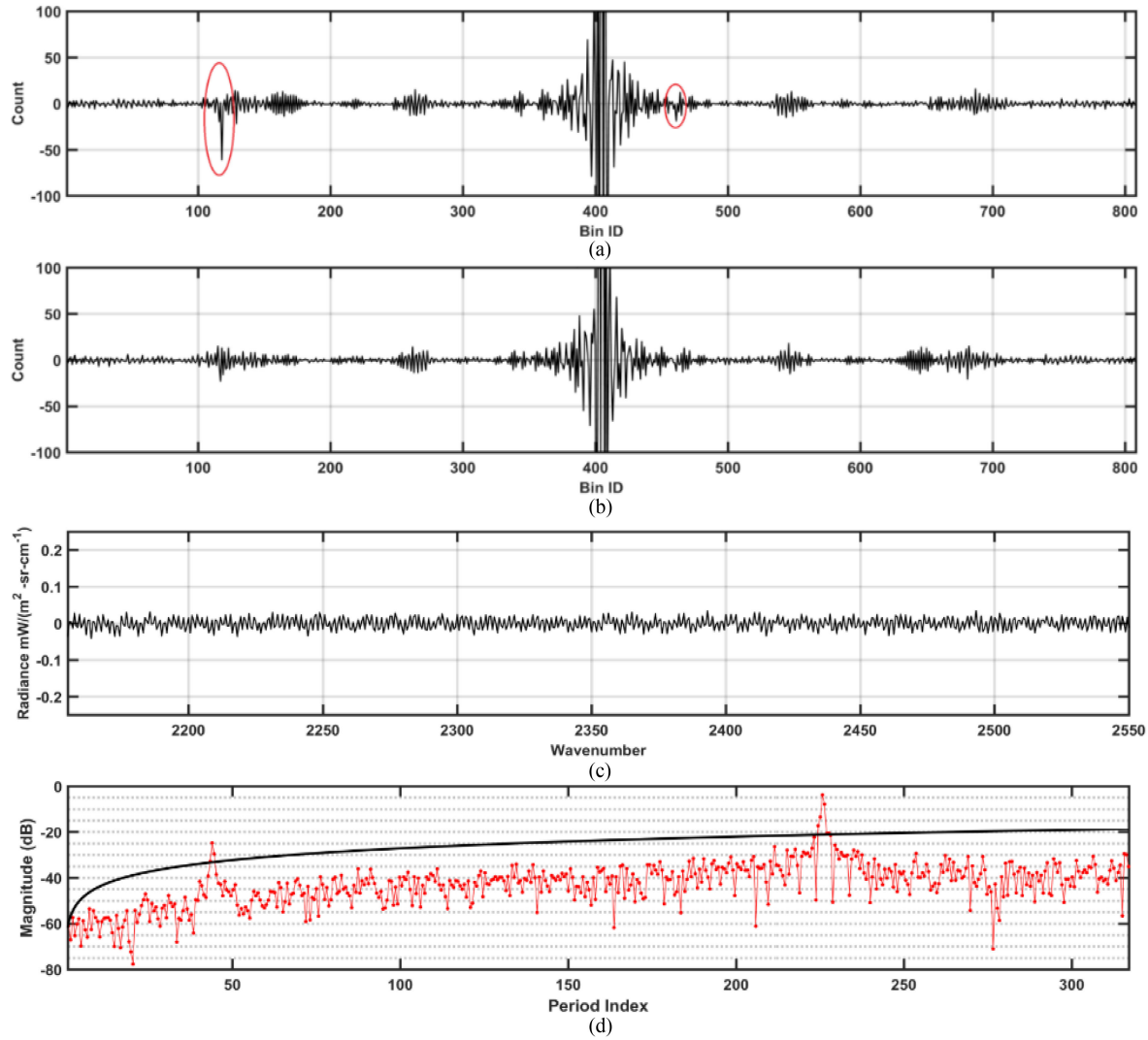

Fig. 10. (a) and (b) are the *I* and *Q* components of an SWIR interferogram corresponding to FOV4/FOR16/SCAN3 in a SNPP CrIS FSR SDR granule started at 06:10:15, March 24, 2019. Two impulse noise events are highlighted on part I interferogram. (c) is the imaginary spectral radiance and (d) is the PSD of this imaginary radiance.

The shutdown of SNPP MWIR sensors during the second quarter of 2019 due to the radiation damage slightly lowers the impulse spike cases, as the result of cooling the internal environment of the instrument. It is reasonable to see such a change because the responsivity of SNPP CrIS SWIR is decreased during the same time. Some weak spikes may not be strong enough to exceed the detection threshold.

On the other hand, compared with the spike detection method based on calibration target measurements in Appendix B, which can detect around 800 SWIR impulse spike events for each day, the daily occurrence of detected impulse spike events in Fig. 11 during the period without abnormal events is below 600. This indicates the reasonability of the detected spike events using the new algorithm. The difference of about 200 detected spike events is observed between the two algorithms primarily because of the high thresholds used in the new algorithm for reducing the occurrence of false alarms. It might indicate the deficiency of the algorithm in detecting some weak spikes.

B. *Impacts on Quality of CrIS Data at the SWIR Band*

The big impact of spikes on the CrIS data has been demonstrated through the simulations in Section II. However, it is not easy to quantify this impact through the CrIS observations because of the difficulty to separate impact of spikes from other error sources on the CrIS data. Here the community radiative transfer model (CRTM) [17] is adopted to quantify the spike impact. Certain errors remain in CRTM simulations due to the model and profile errors, which are in the range of brightness temperature errors due to the spikes unless the spike is extremely strong (see Section II). Even so, two analyzes are conducted below to assess the impact of spikes on the quality of CrIS

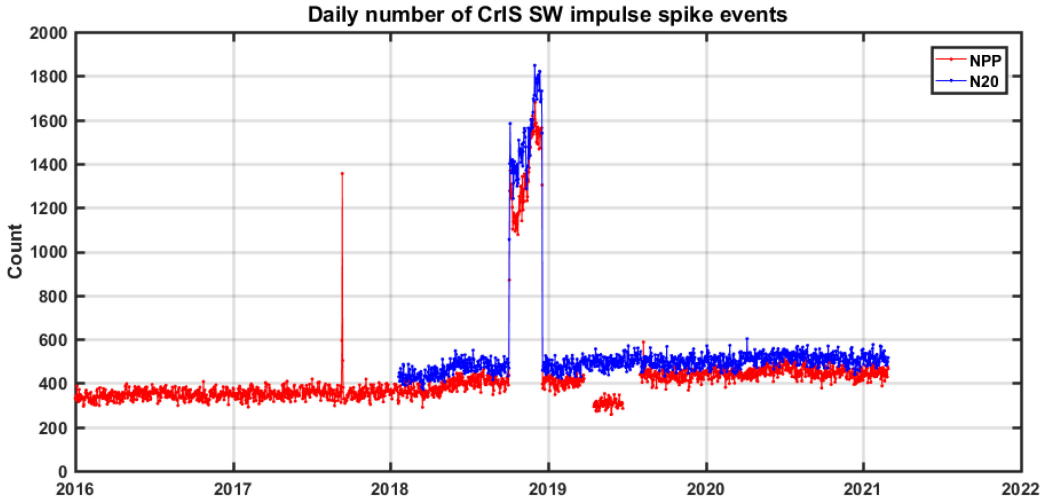

Fig. 11. Daily occurrence of SWIR impulse noise events for SNPP and NOAA-20 CrIS between January 1, 2016 and February 28, 2021.

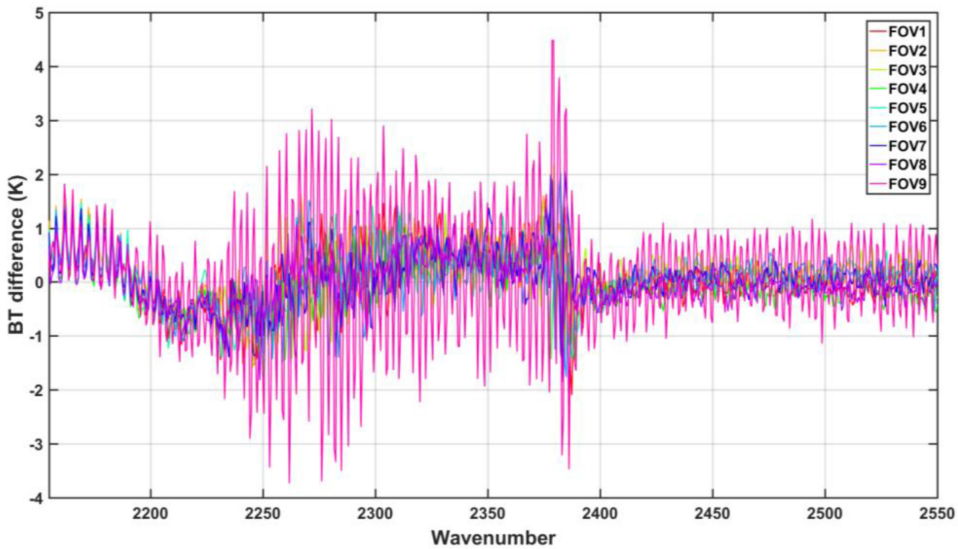

Fig. 12. BT difference between CRTM simulation and observation for a NPP CrIS SWIR FOR 27 at 13:25:41, August 9, 2020. The FOV9 in this FOR is hit by an impulse spike.

SDR data. One is about, one strong nighttime spike case in the CrIS data occurring over open oceans under clear skies, which provides a possibility to assess the difference between the CrIS spectral radiance observations and CRTM simulations. Another is comparing the uncertainty of the CrIS data at the SWIR window channels with/without spikes' contamination.

The CRTM simulation offers a possible approach to assess impact of a very strong spike under clear skies and over open oceans, which was discovered among big datasets from 2018 to 2019, although, the simulations are not typically accurate, particularly in the cloudy conditions. This difference between the observed CrIS spectral radiances and CRTM simulations could be within $+/-$ 3 K over most of the CrIS SWIR band. Fig. 12 is the BT difference between the CRTM simulation and the SNPP CrIS SWIR measurement that was hit by an impulse spike at 13:25:43 P.M. of August 9, 2020. This is a strong event whose spike peak in power spectral domain is 19 units above the threshold. This is a nighttime clear sky case over the North Pacific Ocean, avoiding the uncertainties introduced by nonlocal thermodynamic equilibrium (LTE) [18], surface temperature, and cloud contamination in CRTM simulation. It is clear that the FOV9 shows much wider variability than other FOVs, the differences in window channels are in general around 1 K and more than 3 K in some specific absorbing channels. Notice that this case is labeled as good in overall quality flag in the operational CrIS SDR data stream. This highlights the importance of spike detections from the data to ensure the use of good quality of the data in applications.

In addition to the impact on the quality of the CrIS SDR radiance at the absorption channels within the SWIR band, the

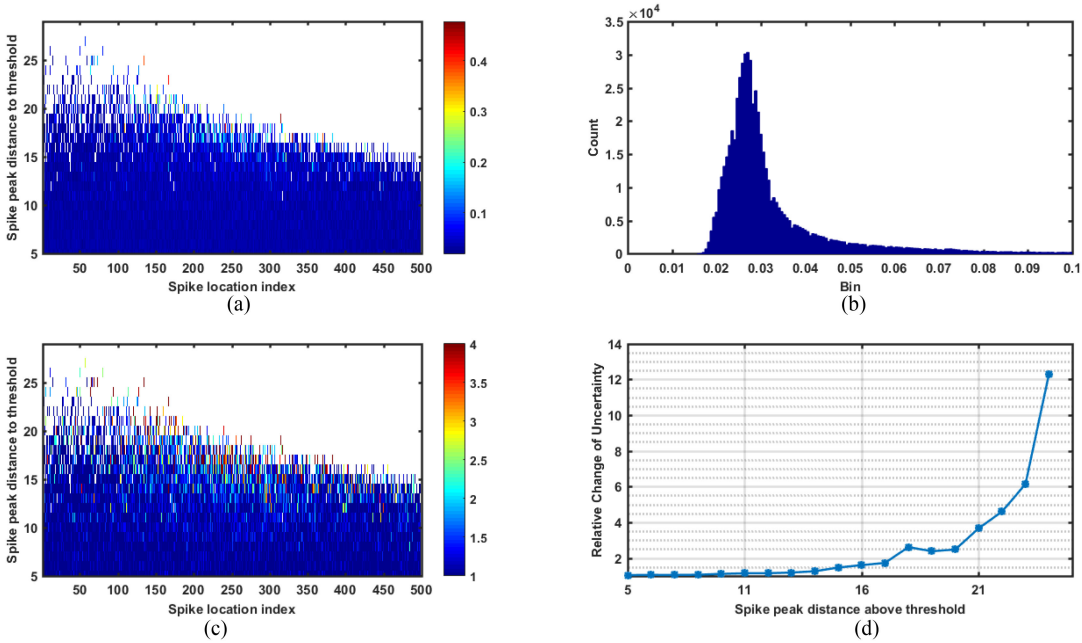

Fig. 13. (a) NPP CrIS SWIR normalized window channel radiance uncertainty between 2400 and 2550 WN against the spike peak location and spike peak distance to threshold in power spectrum domain. (b) Histogram of the baseline normalized window channel radiance uncertainty between 2400 and 2550 WN. (c) Same as (a) but relative to the mean value in (b). (d) Mean relative uncertainty triggered by impulse spikes against spike peak distance to threshold using the data between spike location index 150 and 300 in (c).

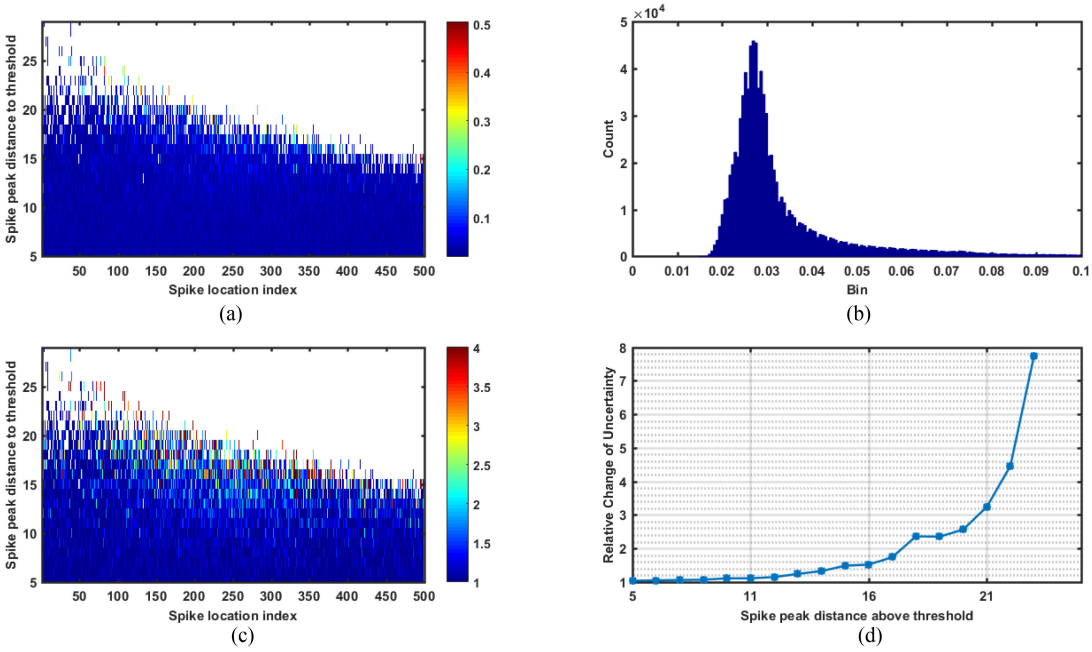

Fig. 14. Same as Fig. 13 but using the N20 CrIS SWIR data.

spikes can increase the uncertainty of the radiance at the window channels inside it. This uncertainty at the SWIR window channel defined the standard deviation of de-trended and normalized real spectral radiance, which is calculated using the following steps:

1) collecting the real component spectral radiance between 2400 and 2550 wavenumbers, marked as $R(i)$, $i = 1, 2, \ldots 241$;
2) conducting a Lag-1 operation to mitigate the impact of the nonstationary feature. $dR(i) = R(i+1) - R(i)$, $I = 1, 2, \ldots, 240$;
3) normalizing the dR series, marked as $dR' = dR/max(abs(dR))$; and
4) calculating the standard deviation of dR', marked as $Y = \mathrm{StdDev}(dR')$.

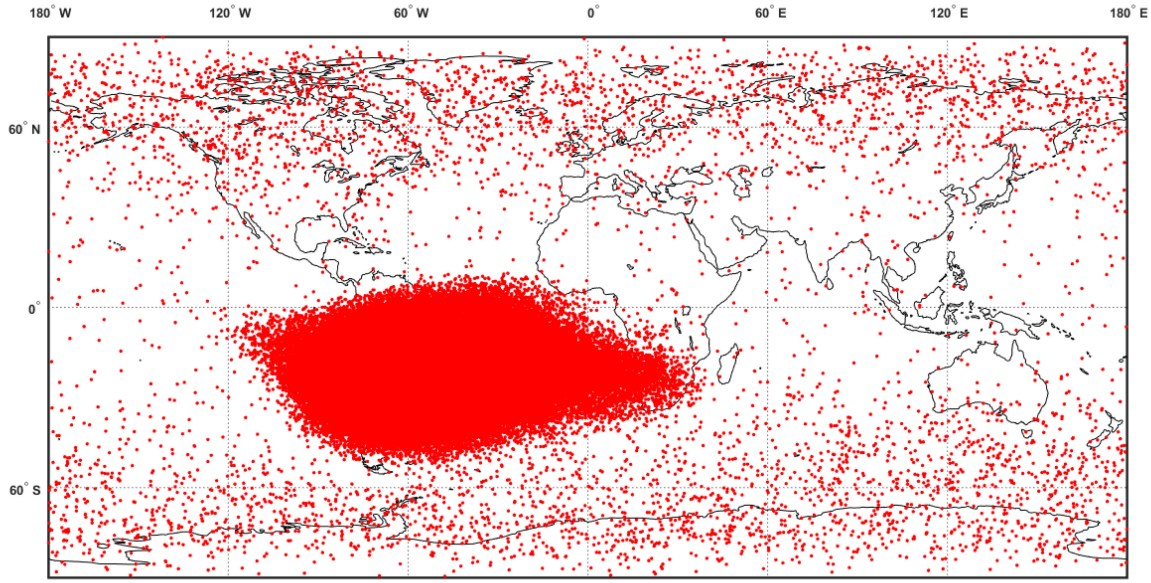

Fig. 15. Location of NPP CrIS SWIR impulse spike events used in Fig. 13.

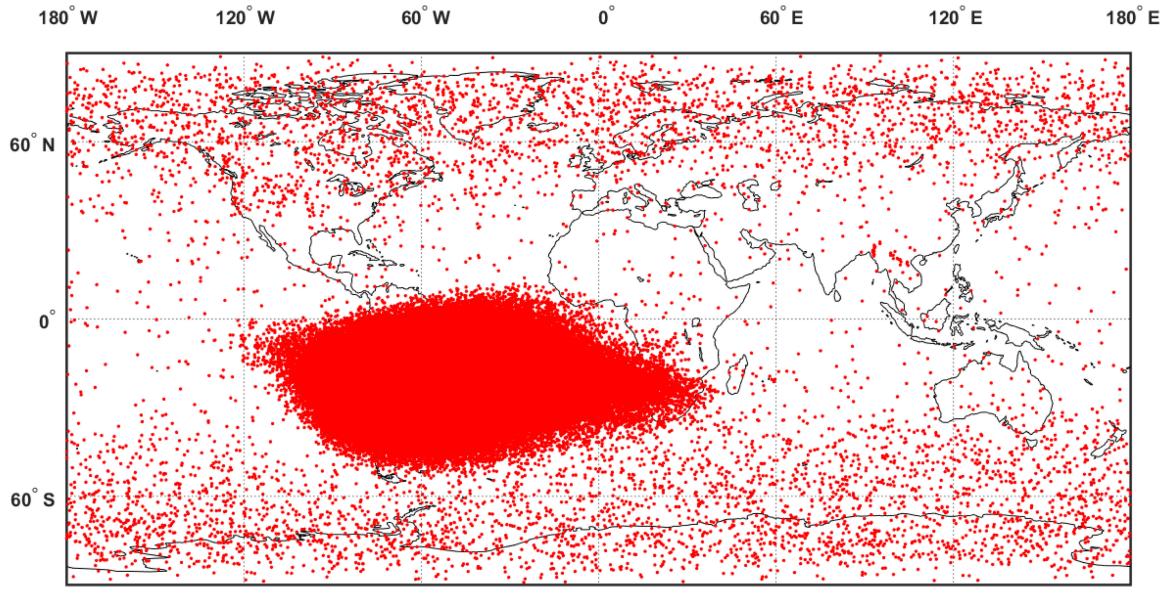

Fig. 16. Location of N20 CrIS SWIR impulse spike events used in Fig. 14.

The preprocessing in the first two steps is similar to that for the imaginary radiance in Section 3 to detrend the data, and the third step is to normalize the reprocessed real radiance. By applying the above processing to the CrIS cloud-free oceanic data in June, August, September of 2018, and December 21, 2019 to March 15, 2020, we obtain the averaged standard deviation of the normalized real spectral radiance at 2400 and 2550 wavenumbers.

Fig. 13(a) shows averaged standard deviations of the above data at 2400 and 2550 wavenumbers (see the color of the pixel) as a function of the location of spike peak (Y-axis) and the distance of spike peak (X-axis) in the PSD domain. Here, the distance denotes the values of spike peak above the reference threshold line generated using (4). The baseline SWIR window channel radiance uncertainty is calculated using spectral radiance of all spike-free FOVs within the same FOR. For example, if one FOV in one FOR is hit by an impulse spike, the other 8 FOVs are selected to calculate the baseline SWIR window channel radiance uncertainty and resultant histogram of these baseline values are plotted in Fig. 13(b). Generally, for a given spike location index, the farther the spike peak distance above the reference are, the higher the standard deviations are. Fig. 13(c) exhibits the normalized standard deviations that are computed by the ratio of the values in Fig. 13(a) to the mean value of

the histogram in Fig. 13(b). A similar conclusion is obtained to that in Fig. 13(a), except for the normalized standard deviation. For a given spike location index, the farther the spike peak distances above the reference are, the higher the normalized standard deviations are. As an example, Fig. 13(d) displays the mean values between spike index 150 and 300 in Fig. 13(c) vs. the spike peak distance to the threshold line. The window channel radiance uncertainty increases exponentially against the spike intensity. The first five values in Fig. 13(d) are 1.04, 1.05, 1.05, 1.06, and 1.11, respectively, showing that even the weakest impulse spike event following our definition could cause 4% uncertainty in the SNPP CrIS SWIR window channels. When a spike peak is 20 units above the threshold line, the window channel radiance uncertainty can be 400% stronger than the baseline value. Considering the much greater sensitivity of absorbing channels to the effect of spikes, the impact of impulse spikes should be seriously considered for users.

Fig. 14 is same as Fig. 13 but for the NOAA-20 CrIS. Data in this plot cover impulse spike cases collected in the following periods: February, March, June, August, and September of 2018, and December 21, 2019 to March 15, 2020. The results are similar with the SNPP CrIS. The first five values in Fig. 13(d) are 1.04, 1.05, 1.06, 1.07, and 1.11, respectively. For strong events whose spike peak is 20 units above the threshold line, the uncertainty can be more than 300% stronger than the baseline value.

The geographic locations of impulse spike events in Figs. 13 and 14 are shown in Figs. 15 and 16, respectively. The geographic pattern of the impulse noise events matches well with the long term SAA observation [19]. No clustering zones are found in any places other than the SAA regions, indicating that the rate of false alarms is pretty low.

V. Conclusion

In this study, a simulation is firstly conducted by using a line-by-line radiative transfer model to understand characteristics of imaginary spectral radiance on the SWIR spectrum in the presence of various spikes with different intensities and hitting locations. The spikes can produce a series of periodic ringing patterns in spectral domain, with more severe ringing in the absorbing channels than the window channels at the SWIR band. The simulations also demonstrate the significant impact of spikes on CrIS data quality at absorbing channels, where the impulse spike impact on BT uncertainty is approximately ten times stronger at absorbing channels than at the window channels.

Furthermore, a new algorithm is developed for detecting spike-contaminated CrIS data based on the ringing features in the imaginary part radiance spectrum. The ringing pattern is better presented as periodic features using the PSD. This method is applied to CrIS FSR spectral data between January 1, 2016 and February 28, 2021 for SNPP and the data between January 20, 2018 and February 28, 2021 for NOAA-20. In the regular conditions, approximately 400 moderate or strong spike events for SNPP and 500 events for NOAA-20 at the SWIR band per day are observed for each of the CrIS instruments. In addition to the impact of spikes on radiance at the CrIS SWIR band through the previous simulation, we conducted a case study to assess the radiance (O) deviation from the CRTM simulation (B) through a very strong spike occurred under a clear sky, nighttime, and open oceans. The O-B bias is larger than 3 K at absorbing channels and around 1 K at window channels within the SWIR band, demonstrating the significant impact of strong spikes on observed CrIS radiance at the SWIR band. In addition, the uncertainty of the de-trended and normalized radiance at the window channels is found to increases exponentially when the spike intensity increases. The weakest spike event causes approximately 4% radiance uncertainty in the window channels; the strong spike event can trigger several times of radiance uncertainty in the window channels.

TABLE III
Information of Two False Impulse Spike Events

Mission	Time	Lat/Lon	Spike location index in PSD	O-B@2500cm^{-1}
N20	11:13:52, 08/19/2018	(50.380, -127.197)	14	15.122 K
SNPP	06:23:41, 03/26/2019	(19.818, 102.495)	13	22.370 K

Presently, the first ten values in the PSD domain are discarded to reduce the false alarms, introduced by very low frequent periodic features added to the SWIR spectrum, caused by reasons other than impulse spikes, which cannot be completely removed through the Lag-1 detrending operation. About 3.2% impulse spike events that hit the kernel zone of the interferogram are missed by this manipulation. Very occasionally, some low frequency drifting pattern extends beyond the first ten counts in the PSD domain, triggering false alarms. Two false spike events are listed in Table III, both of which are forest fire scenes. The low frequency drifting pattern imposed by the very hot upwelling radiance impacts more than ten counts along the x-axis on the PSD plot. But this type of false alarm is easy to detect when compared with CRTM simulation at window channels because a forest fire event usually causes significant difference at SWIR window channels.

Even so, the new algorithm has demonstrated its stable performance in capturing CrIS data that are contaminated by moderate and strong spikes. Therefore, it is expected that the algorithm can offer an approach to flag spike-interference CrIS SDR data in future CrIS SDR operational processing stream.

Appendix A

Generation of normalized PSD function distribution of imaginary radiance

Renormalized PSD distribution of imaginary radiance contains five steps, as described below.

1) Select the SWIR imaginary spectral radiance I_m whose overall quality flag is "good;" here, I_m should contain 637 elements representing the imaginary radiance between 2153.75 and 2551.25 cm^{-1}.
2) Create a new series S using lag 1 difference of I_m. This method could remove the distortion of imaginary spectral

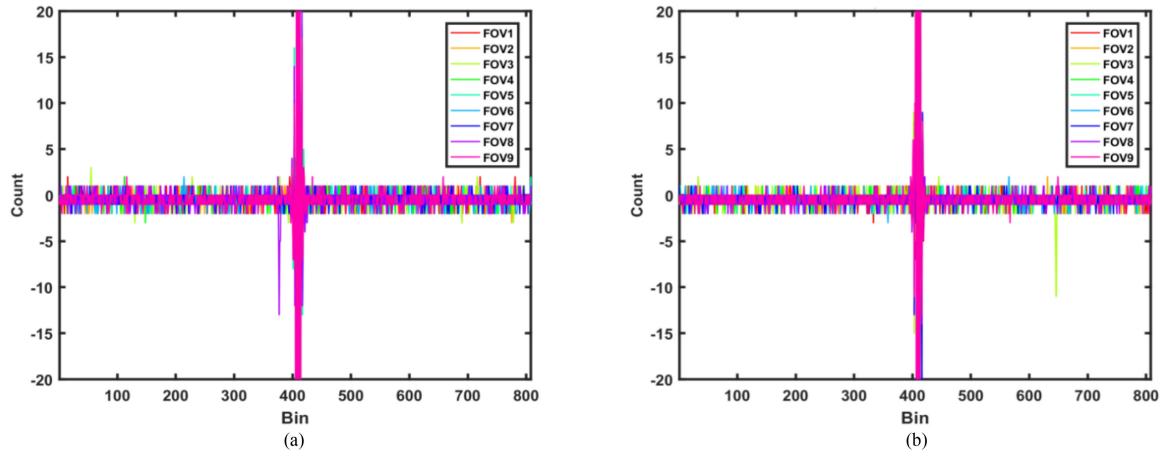

Fig. 17. Two impulse noise events on calibration target: (left) one on internal calibration target (ICT) scene and (right) another on deep space (DS) scene. The data are extracted from a SNPP CrIS RDR granule started at 06:37:50, April 29, 2019.

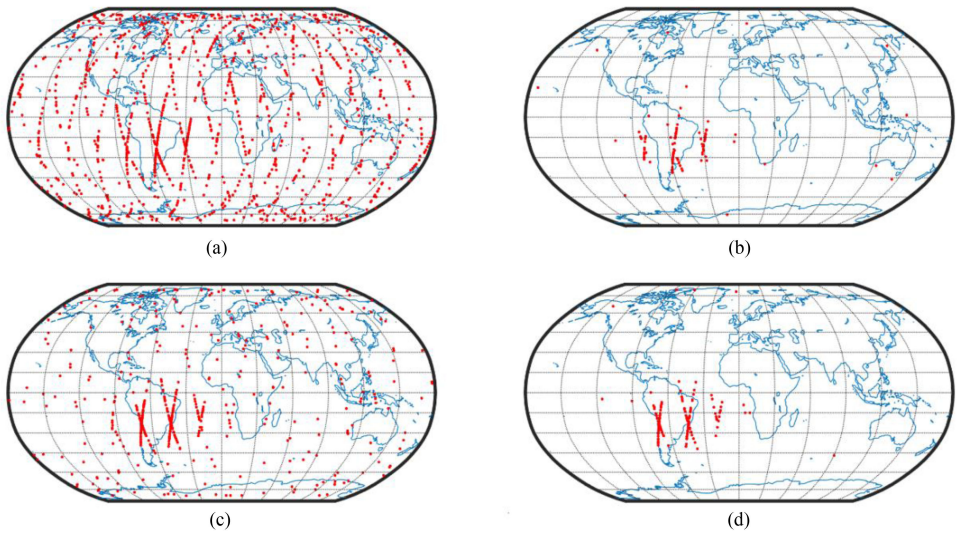

Fig. 18. (Top) Spatial distribution of SNPP CrIS SW calibration interferogram arm with maximal absolute count value greater or equal than (a) 5 and (b) 6. (Bottom) Spatial distribution of NOAA-20 CrIS calibration interferogram arm with maximal absolute value greater or equal than (c) 4 and (d) 5. Data date: April 29, 2019.

radiance caused by very hot scenes, such as sun glints and fire scenes. The imaginary radiance of hot scenes usually shows some nonstationary pattern and it must be removed using the lagged difference method [20]. Otherwise the nonstationary feature will contribute some false alarms in the PSD plot

$$S(i) = I_m(i+1) - I_m(i), I = 1, 2, \ldots, 636. \quad \text{(A.1)}$$

3) Normalize *S* to get a new series *S'* that will be manipulated with PSD

$$S\prime = S/\max(abs(S)). \quad \text{(A.2)}$$

4) Calculate S_{psd}, i.e., the PSD through Fourier transfer

$$S_{psd} = (1/(2 * pi * N)) * abs(fft(S')) \wedge 2. \quad \text{(A.3)}$$

Here, N is the length of S', fft() is the fast Fourier transfer function, *abs(fft(S')).^2* is the dot product of abs(fft(S')) by itself.

5) Plot the logarithmic PSD (in dB) against the period index on the Cartesian coordinate to see the difference between nominal cases and contaminated cases.

Appendix B: Estimating CrIS SWIR Impulse Spikes from Calibration Measurements

Comparing to the earth view interferogram, which has much wider dynamic range when looking at different targets, the calibration views only look at the calibration target, which is much more stable in term of radiative stability. Two impulse spikes are found on each plot of Fig. 17. Another obvious feature of calibration interferogram is the sharp edge of the arm part,

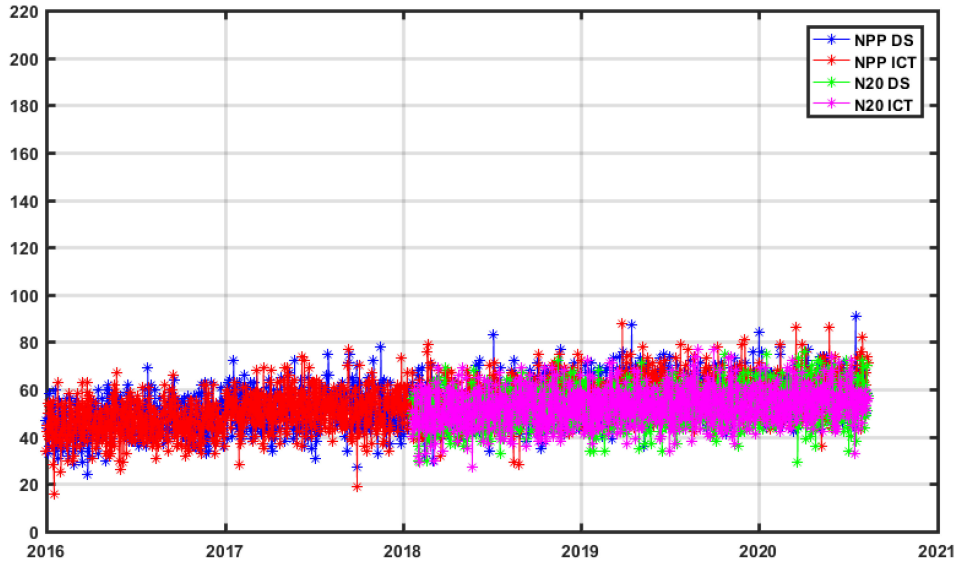

Fig. 19. Daily occurrence of impulse spikes on calibration interferogram between January 1, 2016 and September 30, 2020.

which is due to the signal quantization. A method to detect spike event is conducted by plotting the event location when the maximal absolute value of the interferogram arm exceeds some threshold. The 30 kernel bins, i.e., from 391st to 420th, are excluded in this test.

Since the calibration measurements don't have corresponding geographic location, the nadir position of the scan that the calibration measurements belong to are used. Comparing to Fig. 18(a) and (c), lifting the threshold value one unit higher from five to six for SNPP and from four to five for NOAA-20, inevitably drops some weak impulse spike events, but effectively detects impulse spikes without involving false alarms.

This impulse detection method is applied to the historical data since January 2016 through the end of September 2020. In order to further depress false alarms caused during excessive thermal status, the threshold is lifted to seven for both instruments (see Fig. 19). For SNPP CrIS SWIR, 52 interferogram are confirmed through the DS measurements and 53 through the ICT on average. For NOAA-20 CrIS SWIR, the numbers are 53 for both DS and ICT on average. These numbers are less than half of the impulse spike number shown in Fig. 18(b) and (d). Since there are 30 earth view interferogram and 4 calibration interferogram on each scan, plus considering the 30 kernel, which can also be hit by the impulse spikes, the average daily occurrence of impulse spike events on earth view is 818 for NPP and 826 for N20. Please note that this estimate has already excluded many weak events, which takes more than half of the total counts.

ACKNOWLEDGMENT

The authors would like to thank the JPSS Program for supporting the work associated with the Integrated Calibration and Validation System (ICVS) Project. The manuscript contents are solely the opinions of the author(s) and do not constitute a statement of policy, decision, or position on behalf of the NOAA or the U.S. Government.

REFERENCES

[1] Y. Han *et al.*, "Suomi NPP CrIS measurements, sensor data record algorithm, calibration and validation activities, and record data quality," *J. Geophys. Res. Atmos.*, vol. 118, pp. 12734–12748, Nov. 2013.

[2] R. Eresmaa, J. Letertre-Danczak, C. Lupu, N. Bormann, and A. P. McNally, "The assimilation of cross-track infrared sounder radiances at ECMWF," *Quart. J. Roy. Meteorological Soc.*, vol. 143, no. 709, pp. 3177–3188, Oct. 2017.

[3] M. Goldberg *et al.*, "The global space-based inter-calibration system," *Bull. Amer. Meteorological Soc.*, vol. 92, no. 4, pp. 467–475, Apr. 2011.

[4] G. Chander, T. J. Hewison, N. Fox, X. Wu, X. Xiong, and W. J. Blackwell, "Overview of intercalibration of satellite instruments," *IEEE Trans. Geosci. Remote Sens.*, vol. 51, no. 3, pp. 1056–1080, Mar. 2013.

[5] A. Gambacorta *et al.*, "An experiment using high spectral resolution CrIS measurements for atmospheric trace gases: Carbon monoxide retrieval impact study," *IEEE Geosci. Remote Sens. Lett.*, vol. 11, no. 9, pp. 1639–1643, Sep. 2014.

[6] L. Wang and Y. Chen, "Inter-comparing SNPP and NOAA-20 CrIS toward measurement consistency and climate data records," *IEEE J. Sel. Top. Appl. Earth Observ. Remote Sens.*, vol. 12, no. 7, pp. 2024–2031, Jul. 2019.

[7] Y. Han and Y. Chen, "Calibration algorithm for cross-track infrared sounder full spectral resolution measurements," *IEEE Trans. Geosci. Remote Sens.*, vol. 56, no. 2, pp. 1008–1016, Feb. 2018.

[8] M. W. Kelly, E. J. Ringdahl, A. I. D'Souza, S. D. Luce, and E. W. Cascio, "Proton irradiations of large area Hg1-xCdxTe photovoltaic detectors for the cross-track infrared sounder," *Proc. SPIE Infrared Technol. Appl.*, vol. 4820, pp. 479–490, Jan. 2003.

[9] V. Zavyalov *et al.*, "Noise performance of the CrIS instrument," *J. Geophys. Res. Atmos.*, vol. 118, no. 23, pp. 13108–13120, Dec. 2013.

[10] Y. Chen *et al.*, "Recent improvements for CrIS SDR data quality," Lecture, *Joint Satell. Conf.*, Boston, MA, Sep./Oct. 2019. [Online]. Available: https://ams.confex.com/ams/JOINTSATMET/meetingapp.cgi/Paper/359885

[11] S. A. Clough and M. J. Iacono, "Line-by-line calculation of atmospheric fluxes and cooling rates: 2 Application to carbon dioxide, ozone, methane, nitrous oxide and the halocarbons," *J. Geophys. Res. Atmos.*, vol. 100, pp. 16519–16535, Aug. 1995.

[12] B. E. Rapp, "Engineering mathematics," in *Microfluidics: Modeling, Mechanics, and Mathematics*. Amsterdam, The Netherlands: Elsevier, 2017, ch. 3, pp. 21–50.

[13] D. Tobin *et al.*, "Suomi-NPP CrIS radiometric calibration uncertainty," *J. Geophys. Res. Atmos.*, vol. 118, no. 18, pp. 10589–10600, Sep. 2013.
[14] A. L. Mishev and I. Usoskin, "Assessment of the radiation environment at commercial jet-flight altitudes during GLE 72 on 10 September 2017 using neutron monitor data," *Space Weather*, vol. 16, no. 12, pp. 1921–1929, Dec. 2018.
[15] M. Esplin, B. Esplin, and D. Scott, "Removing radiation-induced spikes from Fourier transform data," in *Proc. Conf. Characterization Radiometric Calibration Remote Sens.*, Logan, UT, USA, Aug. 2017, pp. 1–28.
[16] Y. Chen *et al.*, "Latest improvements for CrIS sensor data records," in *Proc. 22nd Int. TOVS Study Conf.*, Oct./Nov. 2019.
[17] Y. Han *et al.*, "JCSDA community radiative transfer model (CRTM) - Version 1," Nat. Ocean. Atmospheric Admin., Washington, DC, USA, Tech. Rep. NESDIS 122, 2006.
[18] Y. Chen, Y. Han, P. van Delst, and F. Weng, "Assessment of shortwave infrared sea surface reflection and nonlocal thermodynamic equilibrium effects in the community radiative transfer model using IASI data," *J. Atmos. Ocean. Technol.*, vol. 30, no. 9, pp. 2152–2160, 2013.
[19] E. G. Stassinopoulos, X. Michael, and C. A. Stauffer, "Forty-year 'drift' and change of the SAA," NASA Goddard Spaceflight Center, Greenbelt, MD, USA, Rep. NASA/TM-2015-217547, Dec. 2015.
[20] D. Kwiatkowski, P. Phillips, P. C. B. Schmidt, and Y. Shin, "Testing the null hypothesis of stationarity against the alternative of a unit root: How sure are we that economic time series have a unit root?," *J. Econometrics*, vol. 54, no. 1-3, pp. 159–178, Oct.–Dec. 1992.

Xin Jin received the B.S. and M.S. degrees in atmsopherc physics from the Nanjing Institute of Meteorology, Nanjing, China, in 1997 and 2000, respectively, and the Ph.D. degree in atmospheric physics from Peking University, Beijing, China, in 2003.

From 2003 to 2006, he was with the University of Manitoba, Winnipeg, MB, Canada, conducting research on arctic cloud and radiative flux processes. From 2006 to 2011, he was with the Cooperative Institute for Meteorological Satellite Studies, Space Science and Engineering Center, University of Wisconsin, Madison, WI, USA, conducting research on the retrieval of trace gas and the atmospheric profile sounding techniques from geostationary satellites. Since 2011, he has been working on CrIS calibration with NOAA/NEDSIS/STAR.

Banghua Yan received the Ph.D. degree in atmospheric physics from the Institute of Atmospheric Physics, Chinese Academy of Sciences, Beijing, China, in 1997 and the Ph.D. degree in atmospheric radiation from the University of Alaska, Fairbanks, AK, USA, in 2001.

She is currently a Physical Scientist with the Satellite Calibration and Data Assimilation Branch, Center for Satellite Applications and Research (STAR), National Oceanic and Atmospheric Administration (NOAA), Silver Spring, Maryland, USA. From November 1999 to July 2010, she was with the STAR through companies or NOAA Joint Center for Satellite Data Assimilation (JCSDA) or the Earth System Science Interdisciplinary Center, University of Maryland, College Park, MD, USA. During this period, she significantly contributed to the developments of microwave land, snow, and sea ice emissivity models, and microwave satellite instrument data assimilation studies. Those works have significantly improved the use of satellite sounding data in numerical weather prediction (NWP) models. The land, snow, and sea ice microwave emissivity models have been implemented into the NOAA NCEP NWP model and the JCSDA community radiative transfer model that has been successfully used in several operational data assimilation systems in USA. From August 2010 to August 2017, she was an Oceanographer with the NOAA Office of Satellite Data Processing and Distribution, Camp Springs, MD, USA, to lead the NOAA operational ocean color production system. She has authored or coauthored about 30 papers in international peer-reviewed journals.

From September 2017 to September 2019, Dr. Yan successfully led calibrations/validations of the Metop-C Advanced Microwave Sounding Unit-A (AMSU-A) to ensure the operation of AMSU-A data. She also coordinated the JPSS/STAR (JSTAR) Mission Program for more than half year. She is currently leading the calibrations/validations of the Joint Polar Satellite System Ozone Mapping and Profiler Suite (OMPS) and the STAR Integrated Calibration/Validation System (ICVS) Long-term Monitoring.

Ninghai Sun received the Ph.D. degree in atmospheric remote sensing from the University of Maryland, College Park, MD, USA, in 2009.

Since 2002, he has been a Research Scientist with the Center for Satellite Application and Research (STAR), National Oceanic and Atmospheric Administration (NOAA), Silver Spring, MD, USA. He is currently the Technical Lead of Advanced Technology Microwave Sounder (ATMS) Calibration/Validation Team. He is also a Senior Project Engineer/Scientist to develop the JPSS lifecycle reprocessing system for ATMS, CrIS, and OMPS. His research interests include the development of operational satellite microwave instrument calibration theory and remote sensing application retrieval algorithms.

Dr. Sun is the Creator of the STAR Operational Integrated Cal/Val System (ICVS), which is a real time and long term NOAA, NASA, and EUMETSAT meteorological satellites operational status monitoring and calibration system to support NOAA daily operational missions. He is also a Member of the Global Space-based Inter-Calibration System (GSICS) of World Meteorological Organization (WMO), to develop intersatellite calibration algorithm and data product for climate study.

Flavio Iturbide-Sanchez (Senior Member, IEEE) received the B.S.E.E. degree in electronics engineering from Autonomous Metropolitan University, Mexico City, Mexico, in 1999, the M.S.E.E. degree in electrical engineering from the Advanced Studies and Research Center, National Polytechnic Institute, Mexico City, Mexico, in 2001, and the Ph.D. degree in electrical engineering from the University of Massachusetts, Amherst, MA, USA, in 2007.

From 2001 to 2005, he was a Research Assistant with the Microwave Remote Sensing Laboratory, University of Massachusetts, where he was involved in the design, development, and characterization of highly integrated multichip modules and microwave circuits for low-noise, low-power consumption, high-gain, and high-stability microwave radiometers. From 2005 to 2007, he was with the Microwave Systems Laboratory, Colorado State University, Fort Collins, CO, USA, focusing on the demonstration of a low-cost and power-efficient compact microwave radiometer for humidity profiling. From 2008 to 2018, he supported the development of Operational Physical Retrieval Systems that employ hyperspectral-infrared and microwave observations implemented for the Polar Operational Environmental Satellites Project (POES) and the Joint Polar Satellite System (JPSS). Since 2018, he has been a Physical Scientist with NOAA/NESDIS/Center for Satellite Applications and Research, College Park, MD, USA, where he led the calibration and validation of the JPSS cross-track infrared sounder instruments and supports the planning of the next generation of NOAA infrared and microwave sounders. His Ph.D. research was focused on the miniaturization, development, calibration, and performance assessment of low-cost and power-efficient microwave radiometers for remote sensing applications. His research interests include satellite remote sensing, satellite data assimilation, inverse theory applied to geoscience fields, weather forecasting, earth system science, small satellites, and the design of radiometer systems for earth observations based on emerging technologies.

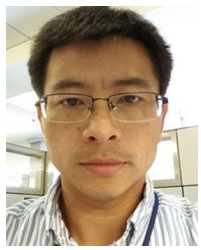

Yong Chen received the B.S. and M.S. degrees in atmospheric sciences from Peking University, Beijing, China, in 1996 and 1999, respectively, and the Ph.D. degree in atmospheric sciences from University of California, Los Angeles, Los Angeles, CA, USA, in 2005.

He is currently a Physical Scientist with NOAA/NESDIS/Center for Satellite Applications and Research, College Park, MD, USA. His research interests include radiative transfer theory and applications, development and implementation of fast radiative transfer model for satellite data assimilation, radiometric and spectral calibration and validation of satellite hyper-spectral infrared sounders, IR data process, and global navigation satellite system radio occultation data processing and data assimilation.